Disturbances Attenuation of Permanent Magnet Synchronous Motor Drives Using Cascaded Predictive-Integral-Resonant Controllers

Zhanqing Zhou, *Student Member, IEEE*, Changliang Xia, *Senior Member, IEEE*, Yan Yan, Zhiqiang Wang, *Member, IEEE*, and Tingna Shi, *Member, IEEE*

***Abstract*—The performance of a standard model predictive controller (MPC) is directly related to its predictive model. If there are unmodeled periodic disturbances in the actual system, MPC will be difficult to suppress the disturbances, thus causing fluctuations of system output. To solve this problem, this paper proposes an improved MPC named predictive-integral-resonant control (PIRC). Compared with the standard MPC, the proposed PIRC could enhance the suppression ability for disturbances by embedding the internal model composing of the integral and resonant loop. Furthermore, this paper applies the proposed PIRC to PMSM drives, and proposes the PMSM control strategy based on the cascaded PIRC, which could suppress periodic disturbances caused by the dead time effects, current sampling errors, and so on. The experimental results show that the PIRC can suppress periodic disturbances in the drive system, thus ensuring good current and speed performance. Meanwhile, the PIRC could maintain the excellent dynamic performance as the standard MPC.**

***Index Terms*—Internal model principle, model predictive control (MPC), periodic disturbances attenuation, permanent magnet synchronous motor, resonant controller.**

I. Introduction

PERMANENT magnet synchronous motor (PMSM) has been widely used in the computer numerical control (CNC) machine tools, elevator control, and traction drive because of the advantages of simple structure, high power factor, and wide speed range [1]–[2]. Model predictive control, as a kind of closed loop control algorithm, has been successfully applied in PMSM control [3]–[4]. Compared with the traditional current vector control strategy, the model predictive controller (MPC)-based PMSM control strategy could improve the dynamic performance of speed and current effectively [5].

The cascaded MPC is an important kind of MPC-PMSM control strategies [6]–[8]. In the cascaded MPC-PMSM systems, both the current and speed loop could be regarded as the single input and single output system which could be simplified as the unconstrained optimization problem, and then their control parameters could be determined offline. Meanwhile, by introducing a posterior constraint, the cascaded MPC could overcome limitations of motion control systems with nonconstrained state feedback controller resulting in low dynamic properties [9].

The design of cascaded MPC can be divided into two parts: the speed loop and the current loop. However, the performance of standard MPC is directly related to the accuracy of the predictive model. Unfortunately, there are several periodic disturbances in the drive system, and their precise mathematical models could not be established. For example, in the speed loop, the current sampling errors will introduce the periodic disturbances into the current feedback channel [10]–[13]. These low-frequency disturbances are usually the major cause of poor speed performance of the standard MPC-based algorithm [6]; in the current loop, the dead time effects of the inverter will introduce periodic disturbances, and these disturbances could lead to stator currents distortion, especially in the case of extreme low speed and heavy load condition [14]–[17]. In summary, the perfect steady-state control performance is usually difficult to realize by using the standard MPC considering the unmodeled disturbances mentioned above.

In recent years, three kinds of improved MPC algorithms are proposed to enhance the inhibition ability of the standard MPC against the unmodeled disturbances, as listed in Table I.

TABLE I
Comparison Between the Different MPC-based Algorithms

	Standard MPC	PRC	Min–max MPC	Offset-free MPC
Stability	Strong	Moderate	Strong	Moderate
Robustness	Poor	Moderate	Strong	Moderate
Disturbances type	Null	Periodic	Non-specific	Constant
Inhibition method	Null	Predictive model	Cost function	Observer
Computational complexity	Low	Relative high	High	Low
Application in motor drive	No-Success	Success [6]	No-Success	Success [5]

Manuscript received November 6, 2016; revised January 19, 2017; accepted March 3, 2017. Date of publication March 7, 2017; date of current version November 2, 2017. This work was supported in part by the National Key Basic Research Program of China (973 Program) under Grant 2013CB035600 and in part by the National Natural Science Foundation of China under Grant 51377121. Recommended for publication by Associate Editor I . Slama-Belkhodja.

Z. Zhou, Y. Yan, and T. Shi are with the School of Electrical and Information Engineering, Tianjin University, Tianjin 300072, China (e-mail: zhzhq@tju.edu.cn; yanyan@tju.edu.cn; tnshi@tju.edu.cn).

C. Xia is with the School of Electrical and Information Engineering, Tianjin University, Tianjin 300072, China, and also with Tianjin Engineering Center of Electric Machine System Design and Control, Tianjin 300387, China (e-mail: motor@tju.edu.cn).

Z. Wang is with Tianjin Engineering Center of Electric Machine System Design and Control, Tianjin 300387, China (e-mail: wangzhq@tju.edu.cn).

Color versions of one or more of the figures in this paper are available online at http://ieeexplore.ieee.org.

Digital Object Identifier 10.1109/TPEL.2017.2679126

The first kind of these algorithms is the predictive repetitive control (PRC), also known as iterative learning MPC [18]–[22]. In PRC, the periodic disturbances are expressed with signal generators in series according to the discrete Fourier theory. In this way, the modified predictive model with periodic disturbances can be established. Using this predictive model, PRC could evaluate the system behavior under periodic disturbances, then the influence of disturbances could be attenuated [18]. PRC is a successful MPC algorithm, but the storage space and computational burden of the PRC will be increased because of the series structure, when a lot of frequencies are contained in the periodic disturbances. Meanwhile, the modified model needs to be updated online to reflect the information of periodic disturbances in real time, so that the control parameters of PRC have also to be calculated online. In addition, the stability of PRC is sensitive to the variation of the frequencies of the disturbances [18]. Therefore, an improved PRC which is insensitive to the frequencies of the disturbances are acquired by connecting the multiple memory loops in series–parallel, but the disturbance attenuation ability of the improved strategy would be weaken [20].

The second kind of algorithms is named min–max MPC [23]–[24]. Instead of the accurate frequency information of disturbances, the only requirement of the min–max MPC is the extreme range of disturbances. In this algorithm, the control law which contents the preset cost function under the worst disturbance condition is determined by solving the min–max optimization problem. However, the min–max MPC can only satisfy the minimum control objectives (such as tracking and stability) in the presence of disturbances, which means the disturbances of outputs are not completely suppressed. Besides, the dynamic programming problem of min–max MPC could hardly be solved online. Thus, the min–max MPC has not been applied in the motor control successfully.

The third kind of algorithms is the offset-free MPC [25]. In this algorithm, the predictive model is augmented with a disturbance model which is used to estimate and predict the mismatch between measured and predicted outputs. The states and disturbances estimated by the Luenberger or Kalman observer are used to initialize the MPC problem. The stability of offset-free MPC could be guaranteed by means of proper design. Meanwhile, compared with PRC, computational burden of offset-free MPC is lower. However, limited by the dynamic performance of the observer, offset-free MPC could only eliminate the disturbance which is constant or varies slowly.

On the basis of the above three kinds of algorithms, this paper proposes an MPC algorithm that can restrain the constant, slow-variation, and periodic disturbances, which is named as the predictive-integral-resonant control (PIRC) algorithm. In the proposed PIRC, the resonant internal model composing of several paralleled quasi-resonant controllers is embedded in the standard MPC algorithm to restrain the periodic disturbances. Compared with PRC, PIRC does not need to store large amount of past time variables, so that the computational complexity is reduced. In addition, PIRC may have relatively strong robustness of frequency, because the resonant internal model can adjust its control bandwidth conveniently. More importantly, the control parameters of the PIRC could be determined offline. Thus, the PIRC can be successfully applied in motor drive systems with rapid transient response. In this paper, a PMSM control strategy-based on the cascaded PIRC is put forward to suppress the ripples of the current and the speed which are introduced by periodic disturbances of dead time effects, current sampling error, and flux harmonics.

II. Periodic Disturbances Attenuation With Integral-Resonant Internal Model

The first-order system including the periodic disturbances is established as follows:

$$\begin{cases} \dfrac{\mathrm{d}x\left(t\right)}{\mathrm{d}t} = Ax\left(t\right) + Bu\left(t\right) + \gamma\left(t\right) \\ y\left(t\right) = Cx\left(t\right) \end{cases} \tag{1}$$

where $x(t)$, $u(t)$, and $y(t)$ represent the state, input, and output variables, respectively; A, B, and C are the corresponding coefficients, respectively; $\gamma(t)$ represents the external periodic disturbances, and it can be expanded as Fourier series as follows:

$$\gamma\left(t\right) = \gamma_0 + \sum_{l=1}^{\infty} a_l \cos\left(l\omega_1 t\right) + \sum_{l=1}^{\infty} b_l \sin\left(l\omega_1 t\right) \tag{2}$$

where γ_0 represents the constant disturbance in control system; a_l and b_l are the Fourier coefficients of cosinoidal and sinusoidal components, respectively; ω_1 is the fundamental angular frequency of $\gamma(t)$.

The Laplace transform of (2) with zero initial condition can be expressed as

$$Y\left(s\right) = C(s\ -\ A)^{-1}\left[BU\left(s\right) + \Gamma\left(s\right)\right] \tag{3}$$

where $Y(s)$, $U(s)$, and $\Gamma(s)$ represent the transform results of $y(t)$, $u(t)$, and $\gamma(t)$, respectively

$$\Gamma\left(s\right) = \frac{\gamma_0}{s} + \sum_{l=1}^{\infty} \frac{a_l s + b_l l\omega_1}{s^2 + \left(l\omega_1\right)^2}. \tag{4}$$

The controller is to be designed to suppress the periodic disturbances $\gamma\ (t)$ and, hence, by the internal model principle [26], the internal model which is constructed by the poles of $\Gamma(s)$ must be embedded in the open-loop transfer function of control system. As can be seen from (4), $s = 0$ and $s = \pm \mathrm{j} l\omega_1$ are the poles of $\Gamma(s)$. Therefore, the required internal model is composed by the following two parts:

1) to suppress constant disturbance, the integral internal model $1/s$ with the pole $s = 0$ is embedded into the forward path between the reference R(s) and Y(s);
2) to suppress periodic disturbances, the periodic internal model $G_\Sigma(s)$ with the poles $s = \pm \mathrm{j} l\omega_1$ $(l = 1, 2, \ldots, \infty)$ is embedded into the forward path between $R(s)$ and $Y(s)$.

The resonant controller can deal with periodic references and disturbances effectively. The transfer function of the ideal resonant controller is

$$G_{\mathrm{R}}\left(s\right) = \frac{K_r s}{s^2 + \left(l\omega_1\right)^2} \tag{5}$$

where K_{r} represents the resonant coefficient, and the resonant frequency is $l\omega_1$. However, the ideal resonant controller

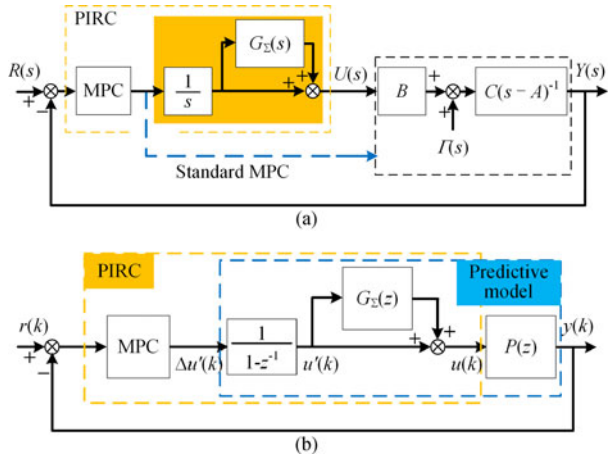

Fig. 1. Control block diagram after embedding the internal model. (a) Control block diagram. (b) Discretization of PIRC.

is difficult to implement in practice, and its frequency robustness is poor [27]. Thus, the quasi-resonant controller is always adopted in the practical applications. The transfer function of quasi-resonant controller is

$$G_{\mathrm{quasi-R}}(s)=\frac{K_{\mathrm{r}}\omega_{\mathrm{c}}s}{s^2+2\omega_{\mathrm{c}}s+(l\omega_1)^2} \tag{6}$$

where ω_{c} is the cut-off frequency of quasi-resonant controller. It can be seen from (6) that $G_\Sigma(s)$ could be constructed by paralleling the quasi-resonant controllers which take $l\omega_1$ as the resonant frequency, namely

$$G_\Sigma(s)=\sum_{l=1}^{\infty}\frac{K_{\mathrm{r},l}\omega_{\mathrm{c}}s}{s^2+2\omega_{\mathrm{c}}s+(l\omega_1)^2}. \tag{7}$$

III. Predictive-Integral-Resonant Control (PIRC)

The control performance of an MPC is directly related to the accuracy of predictive model. Hence, the unmodeled period disturbances in the MPC-based control system would lead to tracking errors or output fluctuations. To solve this problem, the integral and resonant internal model are embedded into the MPC-based control system. However, the predictive model will be changed after embedding the internal model, as it contains the mathematical model of internal model and original control plant simultaneously. In this paper, the integral and resonant internal models are embedded in the MPC-based control system in series, and we rebuild the *predictive model* and *control law* considering the embedded internal model. As a result, an improved MPC named PIRC is gotten, as shown in Fig. 1(a).

A. Predictive Model

Discretize (1) and the result is as follows:

$$\begin{cases}x(k+1)=A_{\mathrm{d}}x(k)+B_{\mathrm{d}}u(k)+\gamma(k)\\ y(k)=Cx(k)\end{cases} \tag{8}$$

where $A_{\mathrm{d}}=\mathrm{e}^{AT_{\mathrm{s}}}$; $B_{\mathrm{d}}=(\int_0^{T_{\mathrm{s}}}\mathrm{e}^{At}\mathrm{d}t)B$; T_{s} represents the discrete control period; k represents the kT_{s} sampling instant.

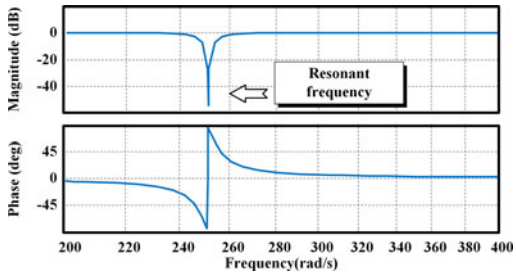

Fig. 2. Bode diagram of $[1+G_\Sigma(z)]^{-1}$.

Transforming (7) into z domain based on Tustin transformation, yields

$$G_\Sigma(z)=\sum_{l=1}^{\infty}\frac{b_{1,l}+b_{2,l}z^{-2}}{1+a_{1,l}z^{-1}+a_{2,l}z^{-2}} \tag{9}$$

where

$$b_{1,l}=\frac{2K_{\mathrm{r},l}\omega_{\mathrm{c}}T_{\mathrm{s}}}{(l\omega_1)^2T_{\mathrm{s}}^2+4\omega_{\mathrm{c}}T_{\mathrm{s}}+4};\ b_{2,l}=\frac{-2K_{\mathrm{r},l}\omega_{\mathrm{c}}T_{\mathrm{s}}}{(l\omega_1)^2T_{\mathrm{s}}^2+4\omega_{\mathrm{c}}T_{\mathrm{s}}+4};$$
$$a_{1,l}=\frac{2(l\omega_1)^2T_{\mathrm{s}}^2-8}{(l\omega_1)^2T_{\mathrm{s}}^2+4\omega_{\mathrm{c}}T_{\mathrm{s}}+4};\ a_{2,l}=\frac{(l\omega_1)^2T_{\mathrm{s}}^2-4\omega_{\mathrm{c}}T_{\mathrm{s}}+4}{(l\omega_1)^2T_{\mathrm{s}}^2+4\omega_{\mathrm{c}}T_{\mathrm{s}}+4}.$$

From (8) and (9), the discretization block diagram of PIRC is obtained, as shown in Fig. 1(b). In order to build the predictive model in Fig. 1(b), first, the state equation in (8) is multiplied by $[1+G_\Sigma(z)]^{-1}$ on the both sides, which is equivalent to embedding the resonant internal model into (8). Then, we have

$$\begin{aligned}&[1+G_\Sigma(z)]^{-1}x(k+1)\\&=[1+G_\Sigma(z)]^{-1}A_{\mathrm{d}}x(k)+B_{\mathrm{d}}u'(k)+[1+G_\Sigma(z)]^{-1}\gamma(k)\end{aligned} \tag{10}$$

where $u'(k)=[1+G_\Sigma(z)]^{-1}u(k)$. The Bode diagram of $[1+G_\Sigma(z)]^{-1}$ is drawn in Fig. 2, where $l=1$, $K_{\mathrm{r}}=1000$, $\omega_{\mathrm{c}}=0.01$ rad/s, $\omega_1=2\pi\times 40$ rad/s.

As shown in Fig. 2, the attenuation effect of $[1+G_\Sigma(z)]^{-1}$ on the resonant-frequency signal is very strong, whereas it has little effect on the signals at other frequency. According to this feature, (10) can be simplified as

$$\begin{cases}x(k+1)=A_{\mathrm{d}}x(k)+B_{\mathrm{d}}u'(k)+\gamma_0\\ y(k)=Cx(k)\end{cases}. \tag{11}$$

Second, (11) is multiplied by the differential operator $\Delta=1-z^{-1}$ on the both sides, which is equivalent to embedding the integral internal model into (11), thus, we can get

$$\Delta x(k+1)=A_{\mathrm{d}}\Delta x(k)+B_{\mathrm{d}}\Delta u'(k). \tag{12}$$

According to (12), the new predictive model can be obtained by augmenting Δx to the state variable, which is

$$\begin{cases}\overbrace{\begin{bmatrix}\Delta x(k+1)\\ y(k+1)\end{bmatrix}}^{\boldsymbol{x}_{\mathrm{m}}(k+1)}=\overbrace{\begin{bmatrix}A_{\mathrm{d}} & 0\\ CA_{\mathrm{d}} & 1\end{bmatrix}}^{\boldsymbol{A}_{\mathrm{m}}}\overbrace{\begin{bmatrix}\Delta x(k)\\ y(k)\end{bmatrix}}^{\boldsymbol{x}_{\mathrm{m}}(k)}+\overbrace{\begin{bmatrix}B_{\mathrm{d}}\\ CB_{\mathrm{d}}\end{bmatrix}}^{\boldsymbol{B}_{\mathrm{m}}}\Delta u'(k)\\ y(k)=\overbrace{\begin{bmatrix}0 & 1\end{bmatrix}}^{\boldsymbol{C}_{\mathrm{m}}}\begin{bmatrix}\Delta x(k)\\ y(k)\end{bmatrix}\end{cases} \tag{13}$$

where $\boldsymbol{x}_{\mathrm{m}}(k)$, $\Delta u'(k)$, and $y(k)$ are the state, input, and output variables of the new predictive model, and $\boldsymbol{A}_{\mathrm{m}}$, $\boldsymbol{B}_{\mathrm{m}}$ and $\boldsymbol{C}_{\mathrm{m}}$ are the corresponding coefficient matrixes.

Comparing the new predictive model with (8), the following changes could be found:

1) the incremental value Δx becomes the state variable instead of the steady value x;
2) $\Delta u'(k)$ becomes the optimal objective instead of $u(k)$;
3) the disturbances term $\gamma(t)$ no longer exists.

B. Control Law

According to (13), the following tracking optimization problem can be established:

$$\min_{\Delta u'(k)} V(k)=\sum_{j=1}^{N} Q_j[r-y(k+j)]^2+\sum_{j=1}^{N} R_j \Delta u'^2(k+j-1)$$

$$\text{s.t.}\quad \boldsymbol{x}_{\mathrm{m}}(k+1)=\boldsymbol{A}_{\mathrm{m}}\boldsymbol{x}_{\mathrm{m}}(k)+\boldsymbol{B}_{\mathrm{m}}\Delta u'(k)$$
$$y(k)=\boldsymbol{C}_{\mathrm{m}}\boldsymbol{x}_{\mathrm{m}}(k) \tag{14}$$

where r is the reference value; $R_j, Q_j \in \mathbf{R}^+$ represent the weight coefficients of input and output at each predictive step; $N \in \mathbf{Z}^+$ is predictive horizon.

From (13), the expression of $y(k+j)$ can be derived as

$$y(k+j)=\boldsymbol{C}_{\mathrm{m}}\boldsymbol{A}_{\mathrm{m}}^{j}\boldsymbol{x}_{\mathrm{m}}(k)+\boldsymbol{C}_{\mathrm{m}}\sum_{i=0}^{j-1}\boldsymbol{A}_{\mathrm{m}}^{i}\boldsymbol{B}_{\mathrm{m}}\Delta u'(k+j-1-i). \tag{15}$$

According to (15), the following equation can be established:

$$\boldsymbol{Y}=\boldsymbol{\Omega}\boldsymbol{x}_{\mathrm{m}}(k)+\boldsymbol{F}\Delta\boldsymbol{U}' \tag{16}$$

where

$$\boldsymbol{Y}=\begin{bmatrix} y(k+1) \\ y(k+2) \\ \vdots \\ y(k+N) \end{bmatrix};\quad \Delta\boldsymbol{U}'=\begin{bmatrix} \Delta u'(k) \\ \Delta u'(k+1) \\ \vdots \\ \Delta u'(k+N-1) \end{bmatrix};$$

$$\boldsymbol{\Omega}=\begin{bmatrix} \boldsymbol{C}_{\mathrm{m}}\boldsymbol{A}_{\mathrm{m}} \\ \boldsymbol{C}_{\mathrm{m}}\boldsymbol{A}_{\mathrm{m}}^{2} \\ \vdots \\ \boldsymbol{C}_{\mathrm{m}}\boldsymbol{A}_{\mathrm{m}}^{N} \end{bmatrix};$$

$$\boldsymbol{F}=\begin{bmatrix} \boldsymbol{C}_{\mathrm{m}}\boldsymbol{B}_{\mathrm{m}} & 0 & \cdots & 0 \\ \boldsymbol{C}_{\mathrm{m}}\boldsymbol{A}_{\mathrm{m}}\boldsymbol{B}_{\mathrm{m}} & \boldsymbol{C}_{\mathrm{m}}\boldsymbol{B}_{\mathrm{m}} & \ddots & \vdots \\ & & \ddots & \\ \boldsymbol{C}_{\mathrm{m}}\boldsymbol{A}_{\mathrm{m}}^{N-1}\boldsymbol{B}_{\mathrm{m}} & \boldsymbol{C}_{\mathrm{m}}\boldsymbol{A}_{\mathrm{m}}^{N-2}\boldsymbol{B}_{\mathrm{m}} & \cdots & \boldsymbol{C}_{\mathrm{m}}\boldsymbol{B}_{\mathrm{m}} \end{bmatrix}.$$

Meanwhile, the cost function in (14) can be rearranged as a compact form like

$$\min_{\Delta\boldsymbol{U}'} \boldsymbol{V}=(\boldsymbol{R}_{\mathrm{ref}}-\boldsymbol{Y})^{\mathrm{T}}\boldsymbol{Q}(\boldsymbol{R}_{\mathrm{ref}}-\boldsymbol{Y})+\Delta\boldsymbol{U}'^{\mathrm{T}}\boldsymbol{R}\Delta\boldsymbol{U}' \tag{17}$$

where $\boldsymbol{R}_{\mathrm{ref}}=\underbrace{[r \quad r \quad \ldots \quad r]^{\mathrm{T}}}_{N}$; $\boldsymbol{Q}=\mathrm{diag}\,[Q_1\, Q_{2\ldots}\, Q_N]^T$; $\boldsymbol{R}=\mathrm{diag}\,[R_1\, R_{2\ldots}\, R_N]^T$.

Substituting (16) into (17), we have

$$\min_{\Delta\boldsymbol{U}'} \quad \boldsymbol{V}=\Delta\boldsymbol{U}'^{\mathrm{T}}\boldsymbol{H}\Delta\boldsymbol{U}'-\Delta\boldsymbol{U}'^{\mathrm{T}}\boldsymbol{G}+\mathbf{const} \tag{18}$$

where $\boldsymbol{H}=\boldsymbol{F}^{\mathrm{T}}\boldsymbol{F}+\boldsymbol{R}$; $\boldsymbol{G}=2\boldsymbol{F}^{\mathrm{T}}\boldsymbol{Q}[\boldsymbol{R}_{\mathrm{ref}}-\boldsymbol{\Omega}\boldsymbol{x}_{\mathrm{m}}(k)]$; **const** represents the items which are independent of $\Delta\boldsymbol{U}'$.

According to the quadratic programming theory, the optimal solution of (18) is

$$\Delta\boldsymbol{U}'=\frac{1}{2}\boldsymbol{H}\boldsymbol{G}^{-1}$$
$$=\left(\boldsymbol{F}^{\mathrm{T}}\boldsymbol{F}+\boldsymbol{R}\right)^{-1}\boldsymbol{F}^{\mathrm{T}}\boldsymbol{Q}\left[\boldsymbol{R}_{\mathrm{ref}}-\boldsymbol{\Omega}\boldsymbol{x}_{\mathrm{m}}(k)\right]. \tag{19}$$

Furthermore, according to the receding horizon control principle [28]

$$\Delta u'(k)=\underbrace{[1\ 0\ \ldots\ 0]}_{N}\Delta\boldsymbol{U}'. \tag{20}$$

At last, it can be seen from Fig. 1(b) that the relationship between $u(k)$ and $\Delta u'(k)$ can be expressed as

$$u(k)=\underbrace{[1+G_{\Sigma}(z)]}_{\substack{\text{Resonant internal}\\ \text{model}}}\cdot\underbrace{\frac{1}{1-z^{-1}}}_{\substack{\text{Integral internal}\\ \text{model}}}\Delta u'(k)$$
$$=[1+G_{\Sigma}(z)]\,[u'(k-1)+\Delta u'(k)]. \tag{21}$$

From (21), the PIRC is equivalent to the combination of *standard MPC* and *parallel resonant internal model*. The parallel internal model in PIRC is used to enhance inhibiting effect of periodic disturbances. Meanwhile, the solving process of the standard MPC in the PIRC is independent on the design of the parallel internal model, which means the design process of the PIRC could be divided into two separate parts, namely the offline solving of standard MPC and the parameter tuning of internal model.

IV. Cascaded PIRC-based Control Strategy for PMSM

To eliminate the periodic fluctuations of current and speed of PMSM, this section proposes a control strategy based on cascade PIRC. In the proposed strategy, the controllers of both current loop and speed loop adopt the PIRC, as shown in Fig. 3.

A. Unmodeled Disturbances and Mathematical Model of Current Loop

The unmodeled *periodic* disturbances of current loop mainly include the *permanent magnet flux harmonics* [29]–[30] and *dead time effects* of voltage source inverter [14]–[17].

While establishing the mathematical model of PMSM, we usually assume that the rotor flux presents ideal sinusoidal distribution in space. However, for the actual motor, it is difficult to achieve ideal sinusoidal flux distribution due to stator teeth notching, magnetic saturation, and manufacturing restrictions so that the permanent magnet flux linkage exists harmonics.

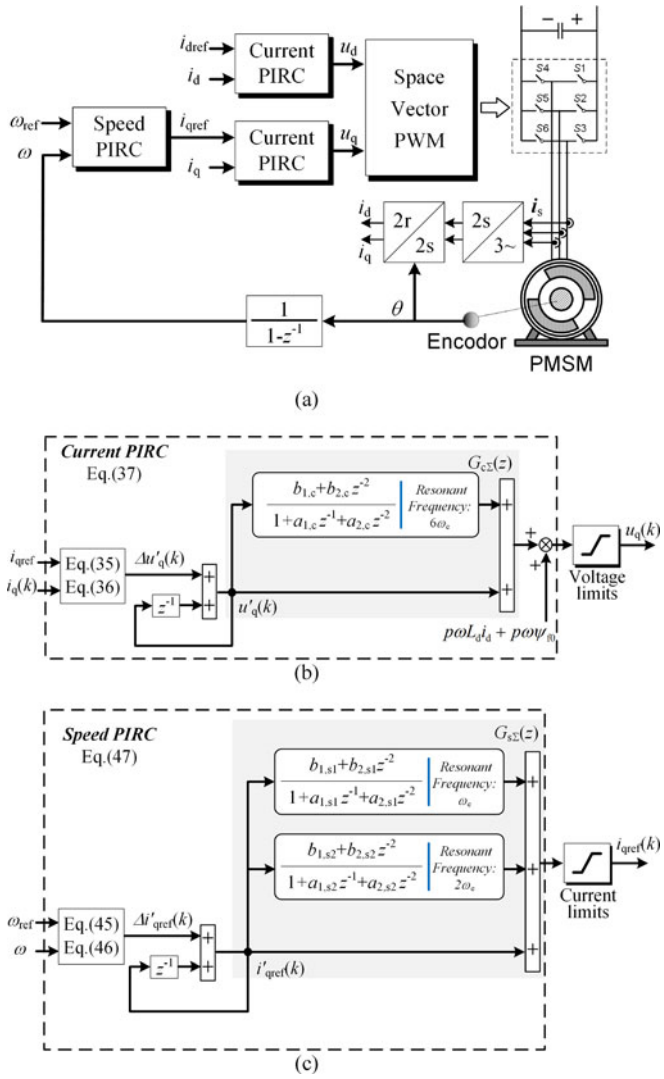

Fig. 3. Proposed cascaded PIRC-based control strategy for PMSM. (a) Control block diagram. (b) Current PIRC. (c) Speed PIRC.

Considering the three-phase symmetry of the motor stator windings, in the case of symmetrical load, there will be no even harmonics in the stator winding. Hence, taking the phase A as an example, the permanent flux linkage can be expressed as

$$\begin{aligned}\psi_{\mathrm{fA}} &= \sum_{l=1}^{\infty} \psi_{\mathrm{f}(2l-1)} \cos\left[(2l-1)\omega_{\mathrm{e}} t\right] \\ &= \psi_{\mathrm{f1}} \cos\omega_{\mathrm{e}} t + \psi_{\mathrm{f3}} \cos 3\omega_{\mathrm{e}} t + \psi_{\mathrm{f5}} \cos 5\omega_{\mathrm{e}} t + \ldots \end{aligned} \quad (22)$$

where ω_{e} donates the electrical angular frequency; ψ_{f1} donates the amplitude of the fundamental waveform of the permanent flux; ψ_{f3} and ψ_{f5} are the amplitude of 3rd and 5th harmonics of the permanent flux. The expression forms of the permanent flux linkage of phase B and C are similar to that of the phase A, only the initial phase angles have differences.

Transforming ψ_{fA}, ψ_{fB}, and ψ_{fC} into the rotating frame, and then the expressions of the permanent magnet flux can be obtained as

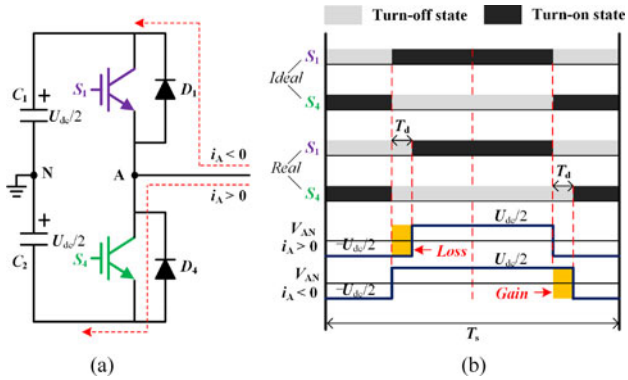

Fig. 4. Schematic diagrams of the dead time effects. (a) Basic configuration of one phase leg during the dead time. (b) Switching patterns and output voltages.

$$\begin{cases} \psi_{\mathrm{fd}} = \psi_{\mathrm{f0}} + \sum_{l=1}^{\infty} \psi_{\mathrm{d}6l} \cos\left(6l\omega_{\mathrm{e}} t\right) \\ \psi_{\mathrm{fq}} = \sum_{l=1}^{\infty} \psi_{\mathrm{q}6l} \cos\left(6l\omega_{\mathrm{e}} t\right) \end{cases} \quad (23)$$

where ψ_{f0} is the dc-component of the permanent magnet flux linkage; $\psi_{\mathrm{d}6l}$ and $\psi_{\mathrm{q}6l}$ are the amplitude of 6lth harmonics. From (23), we can see that the periodic disturbances will appear in ψ_{fd} and ψ_{fq}, and their angular frequencies are $6l\omega_{\mathrm{e}}$.

To avoid shoot-through in the dc link, a time delay called dead time (2–5 μs) should be inserted in the pulse width modulation patterns which guarantees that both switches in an inverter leg will not be conducted simultaneously. The schematic diagrams of the dead time effects are shown in Fig. 4.

From Fig. 4, the average distorted voltage Δu_{AN} caused by the dead time effects are different according to the direction of stator phase current, which has

$$\Delta u_{\mathrm{AN}} = \begin{cases} T_{\mathrm{d}} U_{\mathrm{dc}} / T_{\mathrm{s}}, i_{\mathrm{A}} > 0 \\ -T_{\mathrm{d}} U_{\mathrm{dc}} / T_{\mathrm{s}}, i_{\mathrm{A}} < 0 \end{cases} \quad (24)$$

where U_{dc}, i_{A}, and T_{d} represent the dc-bus voltage, stator current of phase A, and the dead time, respectively.

Furthermore, the average distorted voltages of three phases can be expressed according to the direction of the respective three-phase currents as

$$\Delta u_{\mathrm{At}} = \frac{T_{\mathrm{d}} U_{\mathrm{dc}}}{T_{\mathrm{s}}} \left\{ \frac{2\mathrm{sign}\left(i_{\mathrm{A}}\right) - \mathrm{sign}\left(i_{\mathrm{B}}\right) - \mathrm{sign}\left(i_{\mathrm{C}}\right)}{3} \right\} \quad (25)$$

$$\Delta u_{\mathrm{Bt}} = \frac{T_{\mathrm{d}} U_{\mathrm{dc}}}{T_{\mathrm{s}}} \left\{ \frac{2\mathrm{sign}\left(i_{\mathrm{B}}\right) - \mathrm{sign}\left(i_{\mathrm{C}}\right) - \mathrm{sign}\left(i_{\mathrm{A}}\right)}{3} \right\} \quad (26)$$

$$\Delta u_{\mathrm{Ct}} = \frac{T_{\mathrm{d}} U_{\mathrm{dc}}}{T_{\mathrm{s}}} \left\{ \frac{2\mathrm{sign}\left(i_{\mathrm{C}}\right) - \mathrm{sign}\left(i_{\mathrm{A}}\right) - \mathrm{sign}\left(i_{\mathrm{B}}\right)}{3} \right\} \quad (27)$$

where Δu_{At}, Δu_{Bt}, and Δu_{Ct} are the average distorted voltages of three phases, respectively; i_{A}, i_{B}, and i_{C} are the stator currents of three phases, respectively.

From (25) to (27), the average distorted α- and β-axis voltages $\Delta u_{\alpha\mathrm{t}}$ and $\Delta u_{\beta\mathrm{t}}$ of the stationary reference frame can be drawn in Fig. 5. According to Fig. 5, $\Delta u_{\alpha\mathrm{t}}$ and $\Delta u_{\beta\mathrm{t}}$ can be derived

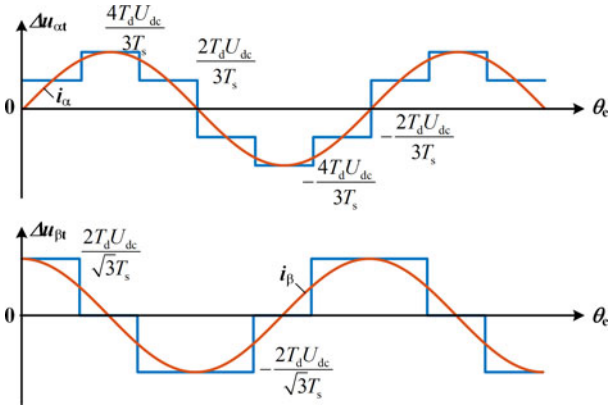

Fig. 5. Distorted voltages and $\alpha\beta$-axis currents of the stationary reference frame.

by taking the Fourier series as follows:

$$\Delta u_{\alpha \mathrm{t}} = \frac{4T_{\mathrm{d}}U_{\mathrm{dc}}}{\pi T_{\mathrm{s}}} \sum_{l=1}^{\infty} \left\{ \frac{1}{6l-5} \sin\left[(6l-5)\,\omega_{\mathrm{e}} t\right] + \frac{1}{6l-1} \sin\left[(6l-1)\,\omega_{\mathrm{e}} t\right] \right\} \tag{28}$$

$$\Delta u_{\beta \mathrm{t}} = \frac{4T_{\mathrm{d}}U_{\mathrm{dc}}}{\pi T_{\mathrm{s}}} \sum_{l=1}^{\infty} \left\{ -\frac{1}{6l-5} \cos\left[(6l-5)\,\omega_{\mathrm{e}} t\right] + \frac{1}{6l-1} \cos\left[(6l-1)\,\omega_{\mathrm{e}} t\right] \right\}. \tag{29}$$

From (28) and (29), the distorted voltages Δu_{dt} and Δu_{qt} of the synchronous reference frame can be obtained by taking the coordinate transformation as follows:

$$\Delta u_{\mathrm{dt}} = \frac{4T_{\mathrm{d}}U_{\mathrm{dc}}}{\pi T_{\mathrm{s}}} \sum_{l=1}^{\infty} \left[\frac{12l}{36l^2-1} \sin\left(6l\omega_{\mathrm{e}} t\right) \right] \tag{30}$$

$$\Delta u_{\mathrm{qt}} = \frac{4T_{\mathrm{d}}U_{\mathrm{dc}}}{\pi T_{\mathrm{s}}} \left\{ -1 + \sum_{l=1}^{\infty} \left[\frac{2}{36l^2-1} \cos\left(6l\omega_{\mathrm{e}} t\right) \right] \right\}. \tag{31}$$

From (30) and (31), Δu_{dt} and Δu_{qt} contain the 6th, 12th, and higher order harmonics due to the dead time effects. It is worth to mention that the nonlinear factors, such as turn-on and turn-off delay of insulated gate bipolar transistor (IGBT), forward voltage drop, etc., have been neglected in the analysis of dead time effects. But, these nonlinear factors have only impact on the amplitude of periodic disturbances and have no effect on the frequencies of disturbances [14].

The *nonperiodic* disturbances of current loop mainly come from the parameter variation of motor [11]. The stator resistance R_{s} varies primarily with winding temperature whereas a small amount of skin and stray loss effects are neglected. In addition, the stator inductances L_{d} and L_{q} are hard to precisely obtain, and they are usually functions of current magnitude and phase angle. For instance, the effects of cross saturation generally result in variations of stator inductances which affects the mathematical model of the motor.

The voltage equations considering the periodic and nonperiodic disturbances can be expressed as follows:

$$\begin{cases} L_{\mathrm{d}} \dfrac{\mathrm{d}i_{\mathrm{d}}}{\mathrm{d}t} = u_{\mathrm{d}} - R_{\mathrm{s}} i_{\mathrm{d}} + p\omega L_{\mathrm{q}} i_{\mathrm{q}} - \Delta L_{\mathrm{d}} \dfrac{\mathrm{d}i_{\mathrm{d}}}{\mathrm{d}t} - \Delta R_{\mathrm{s}} i_{\mathrm{d}} - u_{\mathrm{dt}} \\ L_{\mathrm{q}} \dfrac{\mathrm{d}i_{\mathrm{q}}}{\mathrm{d}t} = u_{\mathrm{q}} - R_{\mathrm{s}} i_{\mathrm{q}} - p\omega L_{\mathrm{d}} i_{\mathrm{d}} - p\omega \psi_{\mathrm{fd}} - \Delta L_{\mathrm{q}} \dfrac{\mathrm{d}i_{\mathrm{d}}}{\mathrm{d}t} - \Delta R_{\mathrm{s}} i_{\mathrm{q}} - u_{\mathrm{qt}} \end{cases} \tag{32}$$

where ΔR_{s}, ΔL_{d}, and ΔL_{q} represent the variations of R_{s}, L_{d}, and L_{q}, respectively. As mentioned above, ΔR_{s} is a function depending on the motor temperature; ΔL_{d} and ΔL_{q} are related to stator current. Therefore, considering the control period is short, the nonperiodic disturbances caused by ΔR_{s}, ΔL_{d}, and ΔL_{q} can be regarded as the slow-variation disturbances. Then, the effects of these nonperiodic disturbances on the performance of current loop can be eliminated by the integral internal model of PIRC.

B. Design of Current PIRC

According to (32), the frequencies of harmonic disturbances are $6l\omega_{\mathrm{e}}$ in the current loop. Therefore, the appropriate resonant internal model could be embedded in the current loop to eliminate the 6*l*th harmonic disturbances. The influence of 12th and higher harmonic disturbances on the current loop are small, so we can take $\omega_1 = 6\omega_{\mathrm{e}}$, $l = 1$ in (9) to eliminate 6th harmonic disturbance. Then, the current PIRC is shown in Fig. 3(b).

After embedding the integral and resonant internal model, the control law of current PIRC will be determined as follows. Taking q-axis as an example, discretize the second equation of (32), and then establish the predictive model of q-axis according to (13). It is worth to note that we adopt the feedforward compensation method to eliminate the cross coupling terms in (32). Then, we have

$$\begin{cases} \overbrace{\begin{bmatrix} \Delta i_{\mathrm{q}}(k+1) \\ i_{\mathrm{q}}(k+1) \end{bmatrix}}^{\boldsymbol{x}_{\mathrm{mq}}(k+1)} = \overbrace{\begin{bmatrix} 1 - R_{\mathrm{s}}T_{\mathrm{s}}/L_{\mathrm{q}} & 0 \\ 1 - R_{\mathrm{s}}T_{\mathrm{s}}/L_{\mathrm{q}} & 1 \end{bmatrix}}^{\boldsymbol{A}_{\mathrm{mq}}} \overbrace{\begin{bmatrix} \Delta i_{\mathrm{q}}(k) \\ i_{\mathrm{q}}(k) \end{bmatrix}}^{\boldsymbol{x}_{\mathrm{mq}}(k)} \\ \quad + \overbrace{\begin{bmatrix} T_{\mathrm{s}}/L_{\mathrm{q}} \\ T_{\mathrm{s}}/L_{\mathrm{q}} \end{bmatrix}}^{\boldsymbol{B}_{\mathrm{mq}}} \Delta u'_{\mathrm{q}}(k) \\ y_{\mathrm{q}}(k) = \overbrace{\begin{bmatrix} 0 & 1 \end{bmatrix}}^{\boldsymbol{C}_{\mathrm{mq}}} \begin{bmatrix} \Delta i_{\mathrm{q}}(k) \\ i_{\mathrm{q}}(k) \end{bmatrix} \end{cases}. \tag{33}$$

Next, according to (14), the corresponding optimization problem for the current PIRC is established as

$$\begin{aligned} \min_{\Delta u'_{\mathrm{q}}(k)} V(k) = & \sum_{j=1}^{N_{\mathrm{cur}}} \left[i_{\mathrm{qref}} - i_{\mathrm{q}}(k+j) \right]^2 \\ & + R_{\mathrm{cur}} \sum_{j=1}^{N_{\mathrm{cur}}} \Delta u_{\mathrm{q}}'^2 (k+j-1) \\ \text{s.t.} \quad & \boldsymbol{x}_{\mathrm{mq}}(k+1) = \boldsymbol{A}_{\mathrm{mq}} \boldsymbol{x}_{\mathrm{mq}}(k) + \boldsymbol{B}_{\mathrm{mq}} \Delta u'_{\mathrm{q}}(k) \\ & y_{\mathrm{q}}(k) = \boldsymbol{C}_{\mathrm{mq}} \boldsymbol{x}_{\mathrm{mq}}(k) \end{aligned} \tag{34}$$

where i_{qref} is the reference current of q-axis, which is produced by the speed PIRC. N_{cur} is predictive horizon of PIRC and determines the range of optimization horizon for the MPC algorithm, and we generally take the value of $N_{\mathrm{cur}}T_{\mathrm{s}}$ larger than motor electrical time constant, namely $N_{\mathrm{cur}} > L_{\mathrm{q}}/T_{\mathrm{s}}R_{\mathrm{s}}$; R_{cur} is the weight coefficient, which is used to avoid the severe changes of $\Delta u'_{\mathrm{q}}$, and then the smooth torque control can be guaranteed.

By solving the optimization problem in (34), we can get

$$\Delta \boldsymbol{U}'_{\mathrm{q}} = \left(\boldsymbol{F}_{\mathrm{q}}^{\mathrm{T}}\boldsymbol{F}_{\mathrm{q}} + \boldsymbol{R}_{\mathrm{cur}}\right)^{-1}\boldsymbol{F}_{\mathrm{q}}{}^{\mathrm{T}}\left[\boldsymbol{i}_{\mathrm{qref}} - \boldsymbol{\Omega}_{\mathrm{q}}\boldsymbol{x}_{\mathrm{mq}}(k)\right] \quad (35)$$

where

$$\boldsymbol{\Omega}_{\mathrm{q}} = [\boldsymbol{C}_{\mathrm{mq}}\boldsymbol{A}_{\mathrm{mq}}\ \boldsymbol{C}_{\mathrm{mq}}\boldsymbol{A}_{\mathrm{mq}}^2\ \ldots\ \boldsymbol{C}_{\mathrm{mq}}\boldsymbol{A}_{\mathrm{mq}}^{N_{\mathrm{cur}}}]^{\mathrm{T}};$$

$$\boldsymbol{R}_{\mathrm{cur}} = \mathrm{diag}\underbrace{[R_{\mathrm{cur}}\ R_{\mathrm{cur}}\ \ldots\ R_{\mathrm{cur}}]}_{\mathrm{N_{cur}}};$$

$$\boldsymbol{i}_{\mathrm{qref}} = \underbrace{[i_{\mathrm{qref}}\ i_{\mathrm{qref}}\ \ldots\ i_{\mathrm{qref}}]^{\mathrm{T}}}_{\mathrm{N_{cur}}};$$

$$\Delta \boldsymbol{U}'_{\mathrm{q}} = [\Delta u'_{\mathrm{q}}(k)\ \Delta u'_{\mathrm{q}}(k+1)\ \ldots\ \Delta u'_{\mathrm{q}}(k+N_{\mathrm{cur}}-1)]^{\mathrm{T}};$$

$$\boldsymbol{F}_{\mathrm{q}} = \begin{bmatrix} \boldsymbol{C}_{\mathrm{mq}}\boldsymbol{B}_{\mathrm{mq}} & 0 & \ldots & 0 \\ \boldsymbol{C}_{\mathrm{mq}}\boldsymbol{A}_{\mathrm{mq}}\boldsymbol{B}_{\mathrm{mq}} & \boldsymbol{C}_{\mathrm{mq}}\boldsymbol{B}_{\mathrm{mq}} & \ddots & \vdots \\ \vdots & \vdots & \ddots & \vdots \\ \boldsymbol{C}_{\mathrm{mq}}\boldsymbol{A}_{\mathrm{mq}}^{N_{\mathrm{cur}}-1}\boldsymbol{B}_{\mathrm{mq}} & \boldsymbol{C}_{\mathrm{mq}}\boldsymbol{A}_{\mathrm{mq}}^{N_{\mathrm{cur}}-2}\boldsymbol{B}_{\mathrm{mq}} & \ldots & \boldsymbol{C}_{\mathrm{mq}}\boldsymbol{B}_{\mathrm{mq}} \end{bmatrix}$$

Then, in accordance with the receding horizon control principle

$$\Delta u'_{\mathrm{q}}(k) = \underbrace{[1\ 0\ \ldots\ 0]}_{N_{\mathrm{cur}}}\Delta \boldsymbol{U}'_{\mathrm{q}}. \quad (36)$$

Finally, according to (21), the control law of current PIRC can be written as

$$\begin{aligned} u_{\mathrm{q}}(k) &= [1 + G_{\mathrm{c}\Sigma}(z)]\left[u'_{\mathrm{q}}(k-1) + \Delta u'_{\mathrm{q}}(k)\right] \\ &\quad + p\omega L_{\mathrm{d}}i_{\mathrm{d}} + p\omega\psi_{f0} \end{aligned} \quad (37)$$

where $G_{\mathrm{c}\Sigma}$ represents the resonant internal model of current PIRC.

C. Unmodeled Disturbances and Mathematical Model of Speed Loop

The unmodeled *periodic* disturbances of speed loop mainly include *current sampling error* [11]–[13] and *flux harmonics* [29]–[30]. Considering the filtering effect of rotor inertia and speed measurement, the amplitude of speed fluctuation caused by flux harmonics is small [31]. So we mainly concern the disturbances introduced by the current sampling errors in the following analysis.

Current feedback is necessary for most motor drive systems. The current measurement procedure, which mainly includes sampling, low-pass filtering, polarity conversion, and calculation, is depicted in Fig. 6, where R_{m} is the sampling resistance, and u_0 is the offset voltage added in the polarity conversion part.

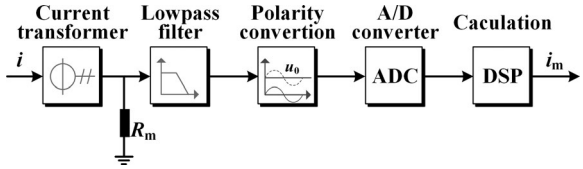

Fig. 6. Schematic of current measurement.

Ignoring nonideal factors in filter and analog-to-digital converter, the acquired current information can be expressed as

$$i_{\mathrm{m}} = \frac{R_{\mathrm{m}}}{R_{\mathrm{mN}}}i + \frac{u_0 - u_{0\mathrm{N}}}{rR_{\mathrm{mN}}} = Ki + i_0 \quad (38)$$

where *r* is the transducer ration of current sensor; R_{mN} and $u_{0\mathrm{N}}$ are the nominal values of sample resistance and offset voltage, respectively.

According to (38), the accuracy of current measurement tends to be affected by mainly two factors. One is the deviation between u_0 and $u_{0\mathrm{N}}$. This deviation is generally caused by unbalanced positive and negative feeding voltage of the sensor and zero voltage drift of the analog devices. The other is the variation of R_{m} caused by temperature rise. These two aspects cause offset and proportion errors between i_{m} and i.

$i_{0\mathrm{A}}$, $i_{0\mathrm{B}}$ and K_{A}, K_{B} are defined as the offset errors and proportional coefficients of currents in phase A and phase B, respectively. i_{mA} and i_{mB} are defined as the measurement values for i_{A} and i_{B}; then

$$\begin{cases} i_{\mathrm{mA}} = K_{\mathrm{A}}i_{\mathrm{A}} + i_{0\mathrm{A}} \\ i_{\mathrm{mB}} = K_{\mathrm{B}}i_{\mathrm{B}} + i_{0\mathrm{B}} \end{cases}. \quad (39)$$

Transform (39) into synchronous rotating coordinate and suppose that $K_{\mathrm{A}} = K_{\mathrm{B}} = 1$, then

$$\begin{cases} \Delta i_{\mathrm{d}} = \dfrac{2}{\sqrt{3}}\sqrt{i_{0\mathrm{A}}^2 + i_{0\mathrm{A}}i_{0\mathrm{B}} + i_{0\mathrm{B}}^2}\sin(\omega_{\mathrm{e}}t + \alpha) \\ \Delta i_{\mathrm{q}} = \dfrac{2}{\sqrt{3}}\sqrt{i_{0\mathrm{A}}^2 + i_{0\mathrm{A}}i_{0\mathrm{B}} + i_{0\mathrm{B}}^2}\cos(\omega_{\mathrm{e}}t + \alpha) \end{cases} \quad (40)$$

where $\Delta i_{\mathrm{q}} = i_{\mathrm{mq}} - i_{\mathrm{q}}$; $\Delta i_{\mathrm{d}} = i_{\mathrm{md}} - i_{\mathrm{d}}$; i_{d} and i_{q} are real current values of d- and q-axis, respectively; i_{md} and i_{mq} are the measurement values for i_{d} and i_{q}, respectively; and α is the angle between stator current vector and rotor position.

When $i_{0\mathrm{A}} = i_{0\mathrm{B}} = 0$, it yields

$$\begin{cases} \Delta i_{\mathrm{d}} = \dfrac{\sqrt{3}}{3}(K_{\mathrm{B}} - K_{\mathrm{A}})I\sin\left(2\omega_{\mathrm{e}}t + \dfrac{\pi}{3}\right) + \dfrac{(2 - K_{\mathrm{A}} - K_{\mathrm{B}})}{2}I \\ \Delta i_{\mathrm{q}} = \dfrac{\sqrt{3}}{3}(K_{\mathrm{B}} - K_{\mathrm{A}})I\sin\left(2\omega_{\mathrm{e}}t + \dfrac{\pi}{3}\right) - \dfrac{\sqrt{3}}{6}(K_{\mathrm{A}} - K_{\mathrm{B}})I \end{cases} \quad (41)$$

where *I* is the amplitude of phase current.

It can be seen from (40) and (41) that the current sampling errors will introduce disturbances into current feedback channels. The frequencies contained in the disturbances are same as and twice of the fundamental frequency. It should be noted that it is difficult to eliminate these disturbances through circuit design techniques, as they mainly come from current sensor itself and working temperature. These periodic disturbances are often the

major cause of poor control performance, and if suitable compensation is not applied, the speed will oscillate in the steady state, particularly at low values.

The first kind of the *nonperiodic* disturbances of speed loop is the *inertia mismatch*. The inertia *J* of a PMSM system, including both rotor and load, is usually a constant during a short-term operation process. However, the inertia of the whole system is time-varying in some special applications [11]. The second kind is the *friction torque.* Friction is the tangential reaction force between two surfaces in contact. *The nonlinear effects of friction are unavoidable and widely exist in drive systems, which may cause steady-state errors and tracking lags.* The third kind is the *load torque*. Torque on the load side is generally deemed as one of the most severe nonperiodic disturbances affecting the dynamic performance. For example, since the transmission mechanism is not an ideal rigid body, mechanical resonance can be easily excited due to the load torque. Speed is inevitably changed when load torque is imposed on the motor.

Considering the periodic and nonperiodic disturbances above, the mechanical equation of PMSM can be expressed as

$$J\frac{\mathrm{d}\omega}{\mathrm{d}t} = 1.5p\psi_{\mathrm{f0}}i_{\mathrm{qref}} + 1.5p\psi_{\mathrm{f0}}\Delta i_{\mathrm{q}} - T_{\mathrm{L}} - T_{\mathrm{fric}} - T_{\mathrm{J}} \quad (42)$$

where T_{fric} represents friction torque; $T_{\mathrm{J}} = \Delta J(\mathrm{d}\omega/\mathrm{d}t)$ represents torque errors caused by the inertia mismatch; ΔJ is the value of mismatch inertia. From (42), it could be known that, on one hand, T_{fric} and T_{L} can be regarded as the constant disturbances due to the variation period of load and friction torque is much longer than the control period. Hence, the impact of T_{fric} and T_{L} on the speed control performance can be eliminated by the integral internal model of PIRC effectively. On the other hand, $T_{\mathrm{J}} \approx 0$ in the static states because of $\mathrm{d}\omega/\mathrm{d}t \approx 0$.

D. Design of Speed PIRC

According to (42), the frequencies of the harmonic disturbances are ω_{e} and $2\omega_{\mathrm{e}}$ in the speed loop. Therefore, the resonant internal model with resonant frequency ω_{e} and $2\omega_{\mathrm{e}}$ [in (9), $\omega_1 = \omega_{\mathrm{e}},\ l = 1, 2$] are embedded in the speed PIRC to suppress the speed fluctuation, as shown in Fig. 3(c).

After embedding the resonant model, the control law of speed PIRC could be determined as follows. First, discretize (42), and then establish the predictive model of speed loop according to (13)

$$\begin{cases} \overbrace{\begin{bmatrix}\Delta\omega(k+1)\\ \omega(k+1)\end{bmatrix}}^{\boldsymbol{x}_{\mathrm{ms}}(k+1)} = \overbrace{\begin{bmatrix}1 & 0\\ 1 & 1\end{bmatrix}}^{\boldsymbol{A}_{\mathrm{ms}}} \overbrace{\begin{bmatrix}\Delta\omega(k)\\ \omega(k)\end{bmatrix}}^{\boldsymbol{x}_{\mathrm{ms}}(k)} + \overbrace{\begin{bmatrix}1.5pT_{\mathrm{s}}\psi_{f0}/J\\ 1.5pT_{\mathrm{s}}\psi_{f0}/J\end{bmatrix}}^{\boldsymbol{B}_{\mathrm{ms}}} \Delta i'_{\mathrm{qref}}(k) \\ y_{\mathrm{s}}(k) = \overbrace{\begin{bmatrix}0 & 1\end{bmatrix}}^{\boldsymbol{C}_{\mathrm{ms}}} \begin{bmatrix}\Delta\omega(k)\\ \omega(k)\end{bmatrix} \end{cases} \quad (43)$$

Next, according to (14), the corresponding optimization problem for the speed PIRC is established as

$$\begin{aligned} \min_{\Delta i'_{\mathrm{qref}}(k)} V(k) = &\sum_{j=1}^{N_{\mathrm{spd}}} \left[\omega_{\mathrm{ref}} - \omega(k+j)\right]^2 \\ &+ R_{\mathrm{spd}} \sum_{j=1}^{N_{\mathrm{spd}}} \Delta i'^2_{\mathrm{qref}}(k+j-1) \\ \text{s.t.}\quad \boldsymbol{x}_{\mathrm{ms}}(k+1) &= \boldsymbol{A}_{\mathrm{ms}}\boldsymbol{x}_{\mathrm{ms}}(k) + \boldsymbol{B}_{\mathrm{ms}}\Delta i'_{\mathrm{qref}}(k) \\ y_s(k) &= \boldsymbol{C}_{\mathrm{ms}}\boldsymbol{x}_{\mathrm{ms}}(k) \end{aligned} \quad (44)$$

where ω_{ref} is the reference value of the mechanical angular frequency; ω is the mechanical angular frequency of motor; N_{spd} is predictive horizon of speed PIRC. We generally take the value of $N_{\mathrm{spd}}T_{\mathrm{s}}$ larger than the mechanical time constant, namely $N_{\mathrm{spd}} > \frac{R_s J}{1.5p\psi_f^2 T_{\mathrm{s}}}$; R_{spd} is the weight coefficient, which is used to avoid the severe changes of $\Delta i'_{\mathrm{qref}}$, and then the smooth speed control can be guaranteed.

By solving the optimization problem in (44), we can get

$$\Delta\mathbf{I}'_{\mathrm{qref}} = \left(\boldsymbol{F}_{\mathrm{s}}^{\mathrm{T}}\boldsymbol{F}_s + \boldsymbol{R}_{\mathrm{spd}}\right)^{-1}\boldsymbol{F}_{\mathrm{s}}{}^{\mathrm{T}}\left[\boldsymbol{\omega}_{\mathrm{ref}} - \boldsymbol{\Omega}_s\boldsymbol{x}_{\mathrm{ms}}(k)\right] \quad (45)$$

where

$$\boldsymbol{F}_{\mathrm{s}} = \begin{bmatrix} \boldsymbol{C}_{\mathrm{ms}}\boldsymbol{B}_{\mathrm{ms}} & 0 & \cdots & 0 \\ \boldsymbol{C}_{\mathrm{ms}}\boldsymbol{A}_{\mathrm{ms}}\boldsymbol{B}_{\mathrm{ms}} & \boldsymbol{C}_{\mathrm{ms}}\boldsymbol{B}_{\mathrm{ms}} & \ddots & \vdots \\ \vdots & \vdots & \ddots & \vdots \\ \boldsymbol{C}_{\mathrm{ms}}\boldsymbol{A}_{\mathrm{ms}}^{N_{\mathrm{spd}}-1}\boldsymbol{B}_{\mathrm{ms}} & \boldsymbol{C}_{\mathrm{ms}}\boldsymbol{A}_{\mathrm{ms}}^{N_{\mathrm{spd}}-2}\boldsymbol{B}_{\mathrm{ms}} & \cdots & \boldsymbol{C}_{\mathrm{ms}}\boldsymbol{B}_{\mathrm{ms}} \end{bmatrix}$$

$$\Delta\boldsymbol{I}'_{\mathrm{qref}} = [\,\Delta i'_{\mathrm{qref}}(k)\ \Delta i'_{\mathrm{qref}}(k+1)\ \ldots\ \Delta i'_{\mathrm{qref}}(k+N_{\mathrm{spd}}-1)\,]^{\mathrm{T}}$$

$$\boldsymbol{R}_{\mathrm{spd}} = \mathrm{diag}\underbrace{[\,R_{\mathrm{spd}}\ R_{\mathrm{spd}}\ \ldots\ R_{\mathrm{spd}}\,]^{\mathrm{T}}}_{N_{\mathrm{spd}}}$$

$$\boldsymbol{\omega}_{\mathrm{ref}} = \underbrace{[\,\omega_{\mathrm{ref}}\ \omega_{\mathrm{ref}}\ \ldots\ \omega_{\mathrm{ref}}\,]^{\mathrm{T}}}_{N_{\mathrm{spd}}}$$

$$\boldsymbol{\Omega}_s = [\,\boldsymbol{C}_{\mathrm{ms}}\boldsymbol{A}_{\mathrm{ms}}\ \boldsymbol{C}_{\mathrm{ms}}\boldsymbol{A}_{\mathrm{ms}}^2\ \ldots\ \boldsymbol{C}_{\mathrm{ms}}\boldsymbol{A}_{\mathrm{ms}}^{N_{\mathrm{spd}}}\,]^{\mathrm{T}}.$$

Then, according to the receding horizon control principle, we can get

$$\Delta i'_{\mathrm{qref}}(k) = \underbrace{[\,1\ 0\ \ldots\ 0\,]}_{N}\Delta\boldsymbol{I}'_{\mathrm{qref}}. \quad (46)$$

Finally, according to (21), the control law of speed PIRC can be written as

$$i_{\mathrm{qref}}(k) = \left[1 + G_{\mathrm{s}\Sigma}(z)\right]\left[i'_{\mathrm{qref}}(k-1) + \Delta i'_{\mathrm{qref}}(k)\right]. \quad (47)$$

where $G_{\mathrm{s}\Sigma}$ represents the resonant internal model of speed PIRC.

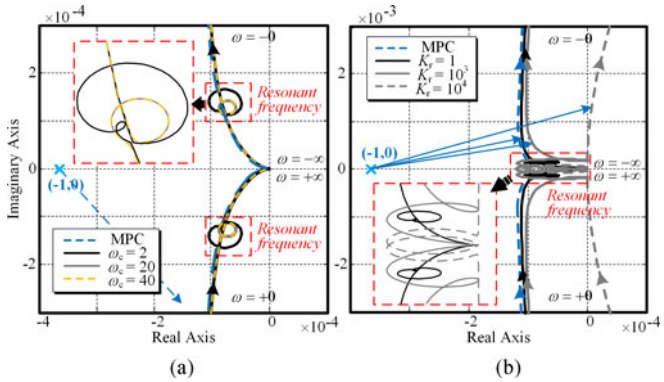

Fig. 7. Nyquist curves of current loop. (a) Influence of ω_c. (b) Influence of K_r.

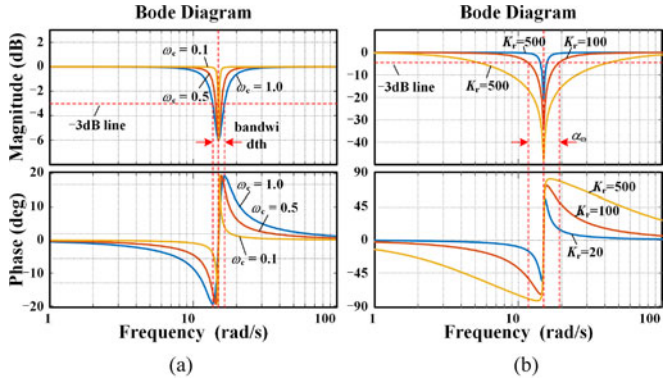

Fig. 8. Bode diagram of $[1 + G_{\mathrm{quasi-R}}]^{-1}$ when the resonant frequency equals to 15 rad/s. (a) $K_r = 2.0/\omega_c$. (b) $\omega_c = 0.1$ rad/s.

V. Stability Analysis

A. Stability Equivalent Conditions Between the Standard MPC and Proposed PIRC

Several literatures show that the closed-loop stability of the standard MPC would be guaranteed if the predictive horizon is long enough [32]. In this section, according to the analysis of Section III, we will give the following equivalent conditions of stability between the standard MPC and proposed PIRC.

Condition 1: $[1 + G_\Sigma(z)]^{-1}$ has strong attenuation effect on the signal that frequencies are equal to the resonant frequencies.

Condition 2: $[1 + G_\Sigma(z)]^{-1}$ has little effect on the amplitude and phase of signals that frequencies are not equal to the resonant frequencies.

The Resonant coefficient K_r and the cut-off frequency ω_c are two important parameters for $G_\Sigma(z)$. To investigate the influence of K_r and ω_c on Conditions 1 and 2, the Nyquist curves of current loop are drawn in Fig. 7. In Fig. 7(a), ω_c is 0.01 rad/s constantly, and K_r is 1, 1×10^3, and 1×10^4, respectively. In Fig. 7(b), K_r is 1 constantly, and ω_c is 2, 20, and 40 rad/s, respectively.

As shown in Fig. 7(a), the gain of resonant internal model on the resonant frequency decreases with the increase of ω_c. However, the system characteristic is not influenced when the signal frequency is not equal to the resonant frequency. So it can be concluded that ω_c has limited effect on the Condition 2.

From the first look to the Fig. 7(b), the stability of the system is improved with the increase of K_r, as the Nyquist curves of the system get more and more far from the key points $(-1, 0)$. However, the characteristic deviation between the PIRC-based system and the MPC-based system get greater with the increase of K_r, which means the resonant internal model also affects the characteristic of the signals beyond the resonant frequency. Therefore, Condition 2 will no longer be established with the overlarge value of K_r, and then the stability of the system is influenced.

According to digital control theory [33], the above stability conditions established in continuous system can still be applied to digital control system. However, the selection of T_s should be carefully considered to reduce the predictive errors caused by discretion, and then guarantees the accurate evaluation of system behavior.

For the PIRC-based PMSM drive system in this paper, the following aspects should be considered during the selection of T_s. 1) The switching frequency of common-type IGBT must not higher than 10 kHz during long-time work, then T_s should be larger than 100 μs. 2) According to the relevant sampling theorem [33], for a system with a rise time on the order of 1 s (which translates to a closed-loop bandwidth on the order of 0.5 Hz), it would be typical to choose a sample rate of 10 to 20 Hz in order to provide some smoothness in the response and to limit the magnitude of control steps. This means that the desired T_s should be shorter than $\pi/(20\omega_b)$, where ω_b denote the bandwidth of control system. In the practical application, a higher sampling rate (shorter control period T_s) is a better choice for ensuring the control performance and saving the design time.

B. Tuning Method of ω_c and K_r Based on the Stability Conditions

1) *Tuning method of* ω_c. According to the analysis of Section V-A, the influence of ω_c on the stability is smaller than K_r. Hence, to achieve the purpose of determining the value of ω_c and K_r separately, we let $K_r = 2.0/\omega_c$ in (6), then we can get

$$G(s) = \frac{2s}{s^2 + 2\omega_c s + (l\omega_1)^2}. \tag{48}$$

From (48), we can see that the amplitude-frequency characteristic of G is independent of K_r. And, the Bode diagram of $[1 + G]^{-1}$ under the condition of $K_r = 2.0/\omega_c$ is shown in Fig. 8(a).

As shown in Fig. 8(a), only the bandwidth of $[1 + G]^{-1}$ becomes larger with the increase of ω_c, which means the value of ω_c has no effect on the Condition 1 when $K_r = 2.0/\omega_c$. Hence, the value of ω_c should be selected as small as possible to meet the requirement of the Condition 2. However, considering the small fluctuations of the angular frequency of the motor, it is necessary to reserve bandwidth to guarantee frequency matching between PIRC and periodic disturbances. For this reason, we assume the fluctuations of the angular frequency of motor is α_ω, and then let $\omega_c = \alpha_\omega$, $K_r = 2.0/\omega_c$ at first. If the PIRC have suppression effect on the periodic disturbances under this condition, then the value of ω_c should be decreased until

TABLE II
PMSM PARAMETERS

Parameter	symbol	value
Rated power	$P_{\rm N}$	6.0 kW
Number of pole-pairs	p	8
Rated speed	$n_{\rm N}$	300 r/min
Rated torque	$T_{\rm N}$	192 N·m
Rated current	$I_{\rm N}$	11.8 A
Permanent magnet flux	$\psi_{\rm f}$	0.9031 Wb
Stator resistance	$R_{\rm s}$	0.76 Ω
Stator inductance	$L_{\rm s}$	13 mH
DC-bus voltage	$U_{\rm dc}$	580 V
Dead time of the inverter	$T_{\rm d}$	3.0 μs
Discrete control period	$T_{\rm s}$	200 μs

the resonant frequencies of PIRC mismatch with the periodic disturbances. Otherwise, the value of $\omega_{\rm c}$ should be increased until PIRC could suppress the periodic disturbances.

2) *Tuning method of* $K_{\rm r}$. After determining the value of $\omega_{\rm c}$, the tuning method of $K_{\rm r}$ is given as follows. From (6), the Bode diagram of $[1+G_{\rm quasi-R}]^{-1}$ when $\omega_{\rm c}=0.1$ rad/s is shown in Fig. 8(b). It can be seen from this figure that the attenuation effect of $[1+G_{\rm quasi-R}]^{-1}$ on the resonant-frequency signal becomes stronger with the increase of $K_{\rm r}$ (see Condition 1). However, $[1+G_{\rm quasi-R}]^{-1}$ also has greater impact on signals whose frequency are not equal to the resonant frequency (see Condition 2). Then, the selection of $K_{\rm r}$ is a compromise between Condition 1 *and* 2**.** In this paper, we first define the frequency range when the amplitude response of $[1+G_{\rm quasi-R}(z)]^{-1}$ smaller than -3 dB as the bandwidth of $[1+G_{\rm quasi-R}(z)]^{-1}$. Second, the corresponding value of $K_{\rm r}$ that could make the bandwidth of $[1+G_{\rm quasi-R}(z)]^{-1}$ equals to α_ω will be considered as the optimal value, as shown in Fig 8(b). It is worth to be mentioned that this tuning process of $K_{\rm r}$ is very complicated. So, MATLAB/Simulink is recommended to determine the value of $K_{\rm r}$ in practical application.

VI. EXPERIMENTAL VERIFICATION

To verify the practicability and validity of PIRC, the experiments are carried out on a 6-kW surface mounted PMSM. The parameters of the motor are given in Table II. In the experimental test bench, a TMS320F28335 Digital Signal Processor (DSP) is employed for algorithm implementation, and the sampling tasks of ac-side currents and dc-side voltage are also accomplished by DSP. Besides, the load is a 11.2-kW induction motor controlled by S120 produced by Siemens. The photo of the implemented system is shown in Fig. 9.

In the following experiments, the PMSM control strategies based on the cascaded MPC and PIRC are implemented, respectively. In order to realize the offset-free tracking for reference current and speed, in the MPC-based control strategy, the integral loop is also embedded in the MPC referring to [34]. While adapting MPC, for the current loop, $R_{\rm cur}=0.01$, $N_{\rm cur}=10$. For the speed loop, $R_{\rm spd}=10$, $N_{\rm spd}=100$. PIRC chooses the same weighting factors and predictive horizons as MPC. In addition, we choose $\omega_{\rm c}=0.05$ rad/s, $K_{\rm r}=50$ unless otherwise stated, and $i_{\rm dref}$ is set to zero for reducing the idling loss of motor in the following experiments. At last, it is worth to mention that the discrete control period and sample period of algorithm are identical in this paper.

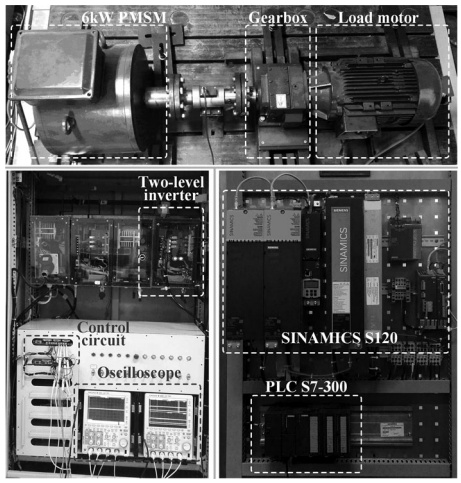

Fig. 9. Photo of the implemented system.

Fig. 10 shows the dynamic experimental waveforms when adopting the PIRC-based control strategy, respectively. In the experiments, the reference value of the electrical angular frequency $\omega_{\rm e,ref}$ is employed as the basis of disturbance frequency, instead of the actual angular $\omega_{\rm e}$. For example, the resonant frequency of current loop is set as $6\omega_{\rm e,ref}$, and the resonant frequency of speed loop is set as $\omega_{\rm e,ref}$ and $2\omega_{\rm e,ref}$.

As shown in Fig. 10(a), when the reference speed changes from 50 to 100 r/min abruptly, the resonant internal model has no restraint effect due to the difference between resonant frequency and disturbance frequency, and then PIRC transforms into MPC so that the PIRC could track the reference speed rapidly. As shown in Fig. 10(b), when the load is increased from 0 to 50 N·m abruptly, speed will exist small fluctuations, but the actual speed could track its reference well due to the good dynamic adjustment ability of the predictive algorithm so that the fluctuations of speed and current could be eliminated rapidly. The above phenomenon indicates that the PIRC could suppress the periodic disturbances by employing the resonant internal model, but it can still retain the same excellent dynamic performance as the MPC.

Fig. 11 shows the waveforms about $i_{\rm A}$, $i_{\rm d}$, $i_{\rm q}$, and its reference $i_{\rm qref}$. In the experiments, PMSM operates at 100 r/min and the load is 100 N·m.

As shown in Fig. 11, the periodic disturbances of the six times electrical angular frequency will be apear in the stator currents beacuse of the dead time effects and flux harmonics. When using the MPC-based control strategy, the average fluctuation of $i_{\rm q}$ is 4 A, and the 2nd and 6th harmonics of the stator currents are high, which causes the distortion of the stator current. Among them, the 2nd harmonic is mainly introduced by the current sampling error, and the 6th harmonic is mainly caused by the dead time effects and flux harmonics. When using PIRC-based control strategy:

1) $i_{\rm q}$ can effectively track its reference $i_{\rm qref}$.

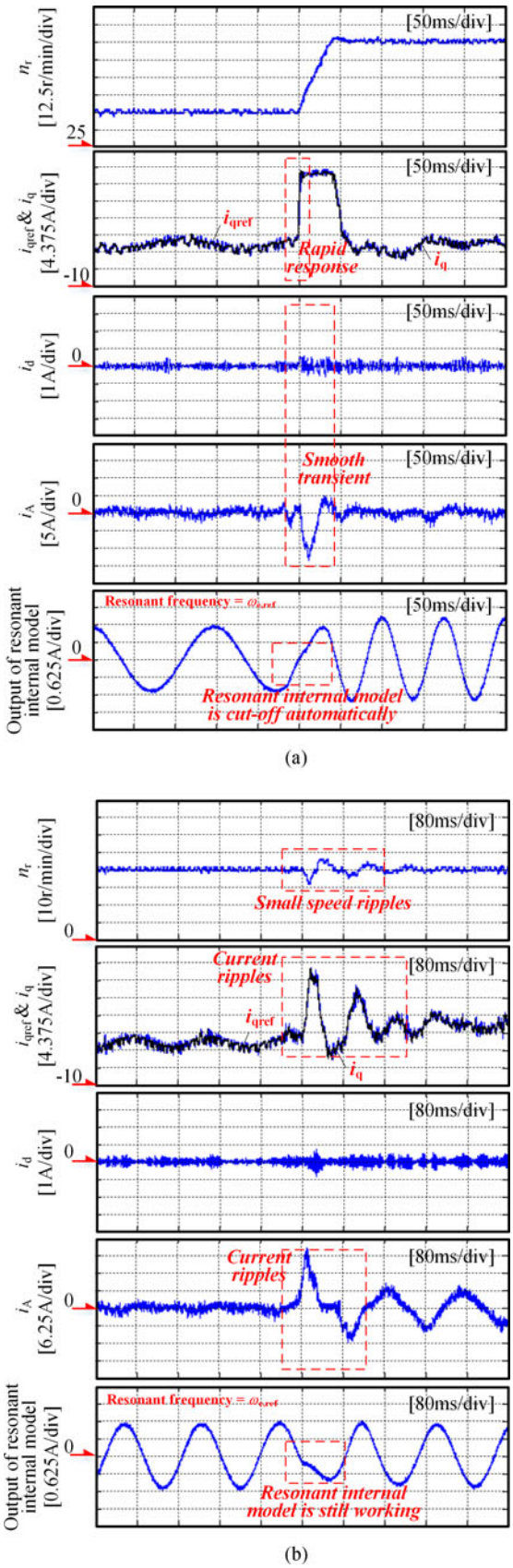

Fig. 10. Dynamic experimental waveforms. (a) Reference speed change. (b) Load torque change.

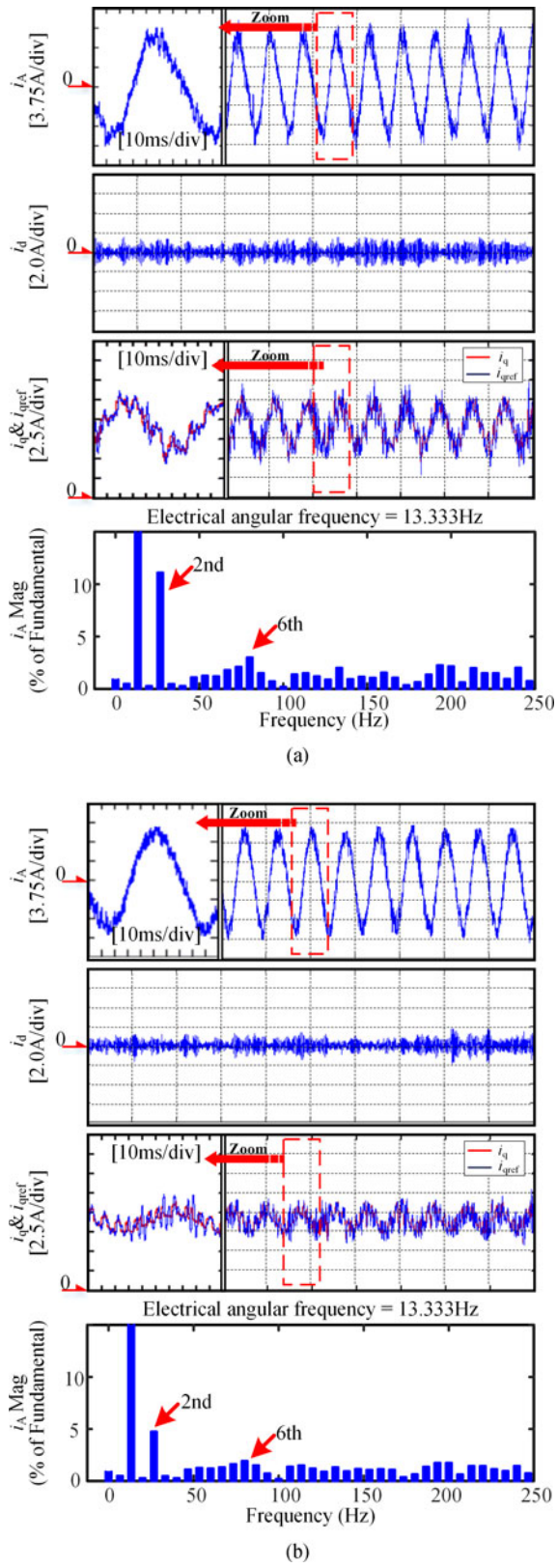

Fig. 11. Performance of current controller under the steady state. (a) MPC-based control strategy. (b) PIRC-based control strategy.

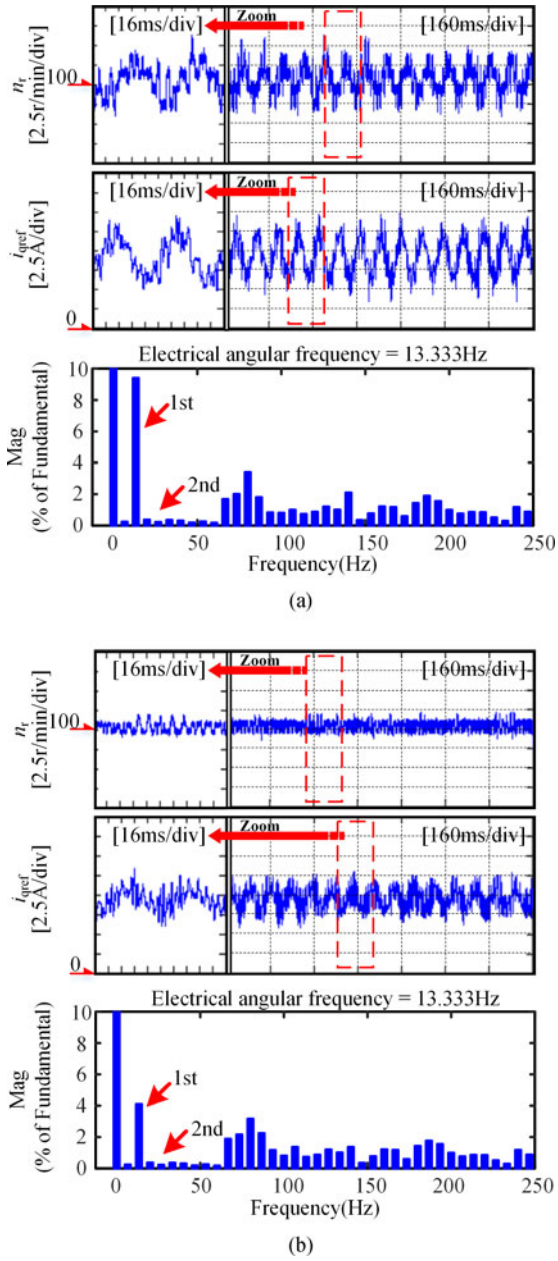

Fig. 12. Performance of speed controller under the steady state. (a) MPC-based control strategy. (b) PIRC-based control strategy.

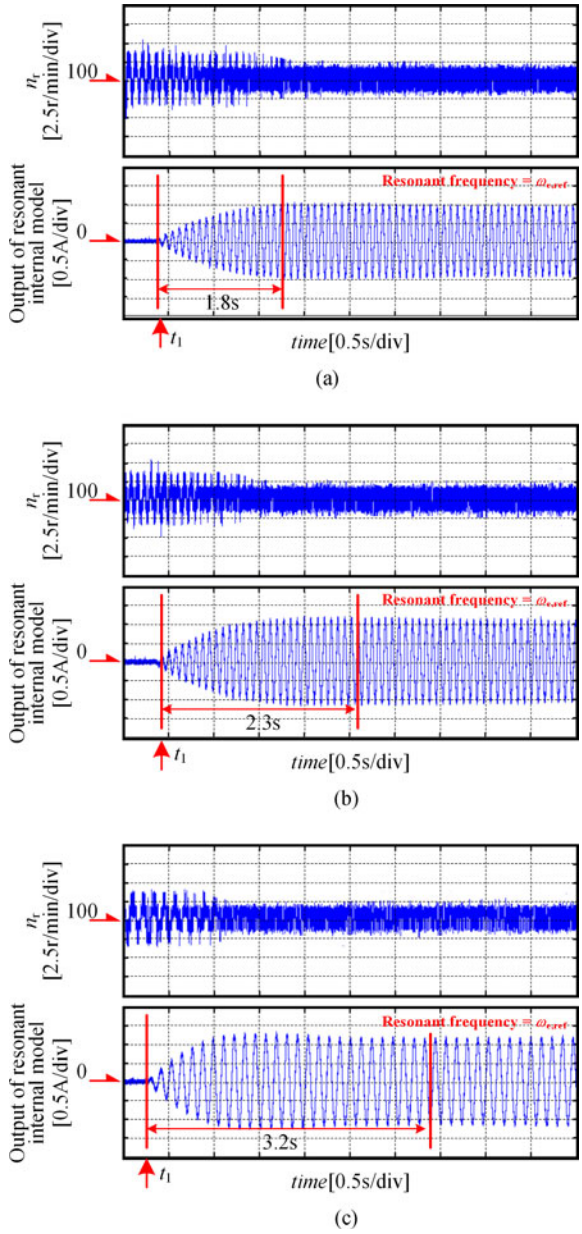

Fig. 13. Performance of speed PIRC controller under different parameters. (a) $\omega_c = 0.01$ rad/s, $K_r = 250$. (b) $\omega_c = 0.05$ rad/s, $K_r = 50$. (c) $\omega_c = 0.1$ rad/s, $K_r = 25$.

2) The 6th harmonic of the stator currents can be effectively suppressed because the current PIRC contains the 6th resonant internal model. Compared with the MPC, the content of 6th harmonic drops by about 20% in the stator currents.
3) Beause the speed PIRC contains the 1st and 2nd resonant internal model, the more stable q-axis reference current is obtained. As a result, the average fluctuations of i_q are reduced to 2.5 A and reduced by 37.5%. The quality of stator current waveform is improved.

Fig. 12 shows the waveform of n_r and i_{qref} when using an MPC-based and PIRC-based strategy, respectively. In the experiments, PMSM operates at 100 r/min, and the load is 100 N·m.

As shown in Fig. 12, when using an MPC-based strategy, the speed exists 13-Hz periodic fluctuations under the influence of the current sampling error and the average fluctuation amplitude is about 4 r/min. When using PIRC-based strategy proposed in this paper: 1) the speed can effectively track its reference. 2) As speed PIRC contains the 1st and 2nd resonant internal model, compared with MPC, the 1st harmonic of speed drops by about 60% according to the fourier decomposition for speed waveform, and then the more stable speed control performance has been achieved.

Fig. 13 shows the experimental waveforms with speed PIRC under the different parameters. In the experiments, different

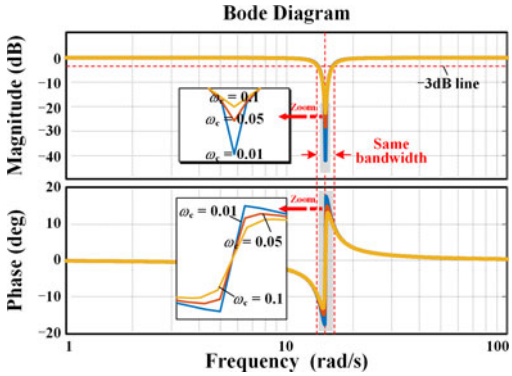

Fig. 14. Bode diagram of $[1+ G_\Sigma(z)]^{-1}$ under the three experimental parameters sets.

ω_c and K_r of speed PIRC are selected according to the tuning method in Section V-B. For example, while selecting $\omega_c = 0.01$ rad/s, and substituting this value into (6), the expected $K_r$is the vlaue which could make the bandwidth of $[1 + G_\Sigma(z)]^{-1}$ equal to $\alpha_\omega = 1.5$ r/min $\times 2 \times \pi/30 = 0.314$ rad/s according to the proposed tuning method. By MATLAB/Simulink, we can obtain the corresponding value of K_r which is equal to 250 approximately. In the same way, the values of K_r corresponding to $\omega_c = 0.05$ rad/s and 0.1 rad/s can be obtained, and their values are 50 and 25, respectively. The Bode diagrams of $[1 + G_\Sigma(z)]^{-1}$ under these different parameters are shown in Fig. 14. From this figure, we can see that the bandwidth of $[1 + G_\Sigma(z)]^{-1}$ for the three parameter-sets are identical with the proposed tuning method. The only difference is, the greater ω_c is, the greater characteristics deviation between (6) and (5) is. As a result, the amplitude-frequency response at the resonant frequency decreases with the increase of ω_c, which lead to the convergence time of the resonant internal model increasing, as shown in Fig. 13. Therefore, a smaller ω_c should be selected preferentially in the practical applications.

VII. Conclusion

This paper proposes the PIRC that can effectively suppress the *constant*, *slow-variation,* and *periodic* disturbances. And, the PIRC has been applied in the PMSM drive system in this paper. Experimental results have verified that the periodic disturbances caused by the dead time effects and the current sampling error are suppressed effectively with the help of PIRC. There are the following two main contributions in this paper.

1) The *predictive model* and the *control law* of the PIRC are given. In order to enhance the inhibition ability of the periodic disturbances, the resonant internal model is embedded in the standard MPC, which formed the PIRC.
2) A PMSM control strategy-based on the cascaded PIRC is proposed, and relevant stability conditions have been given. Furthermore, the detailed parameter tuning methods of the PIRC in PMSM drive system have also been analyzed in this paper.

References

[1] C. Xia, S. Wang, Z. Wang, and T. Shi, "Direct torque control for VSI–PMSMSs using four-dimensional switching-table," *IEEE Trans. Power Electron.*, vol. 31, no. 8, pp. 5774–5785, Nov. 2016.
[2] M. H. Vafaie, B. M. Dehkordi, P. Moallem, and A. Kiyoumarsi, "A new predictive direct torque control method for improving both steady-state and transient-state operations of the PMSM," *IEEE Trans. Power Electron.*, vol. 31, no. 5, pp. 3738–3753, May 2016.
[3] T. J. Besselmann, S. Almér, and H. J. Ferreau, "Model predictive control of load-commutated inverter-fed synchronous machines," *IEEE Trans. Power Electron*., vol. 31, no. 10, pp. 7384–7393, Oct. 2016.
[4] W. Wang, J. Zhang, and M. Cheng, "Common model predictive control for permanent-magnet synchronous machine drives considering single-phase open-circuit fault," *IEEE Trans. Power Electron.*, vol. 32, no. 7, pp. 5862–5872, Jul. 2017.
[5] S. Mariethoz, A. Domahidi, and M. Morari, "High-bandwidth explicit model predictive control of electrical drives," *IEEE Trans. Ind. Appl.*, vol. 48, no. 6, pp. 1980–1992, Nov./Dec. 2012.
[6] S. Chai, L. Wang, and E. Rogers, "A cascade MPC control structure for a PMSM with speed ripple minimization," *IEEE Trans. Ind. Electron.*, vol. 60, no. 8, pp. 2978–2987, Aug. 2013.
[7] C. Garcia, J. Rodriguez, C. Silva, C. Rojas, P. Zanchetta, and H. Abu-Rub, "Full predictive cascaded speed and current control of an induction machine," *IEEE Trans. Energy Convers.*, vol. 31, no. 3, pp. 1059–1067, Apr. 2016.
[8] J. Sawma, F. Khatounian, E. Monmasson, L. Idkhajine, and R. Ghosn, "Cascaded dual-model-predictive control of an active front-end rectifier," *IEEE Trans. Ind. Electron.*, vol. 63, no. 7, pp. 4604–4614, Jul. 2016.
[9] T. Tarczewski and L. M. Grzesiak, "Constrained state feedback speed control of PMSM based on model predictive approach," *IEEE Trans. Ind. Electron.*, vol. 63, no. 6, pp. 3867–3875, Nov. 2016.
[10] C. Xia, B. Ji, and Y. Yan, "Smooth speed control for low speed high torque permanent magnet synchronous motor using proportional integral resonant controller," *IEEE Trans. Ind. Electron.*, vol. 62, no. 4, pp. 2123–2134, Apr. 2015.
[11] J. Yang, W.-H. Chen, S. Li, L. Guo, and Y. Yan, "Disturbance/uncertainty estimation and attenuation techniques in PMSM drives—A survey," *IEEE Trans. Ind. Electron.*, vol. 64, no. 4, pp. 3273–3285, Apr. 2017.
[12] H. Tamura, J. Itoh, and Y. Noto, "Two methods for compensating motor-current-sensor offset error by using DC-voltage component included in phase-voltage command for current-controlled PMSM drive," in *Proc. 17th Eur. Conf. Power Electron. Appl.*, 2015, pp. 1–10.
[13] D. Diallo, S. Diao, and C. Delpha, "Current sensor fault estimation in the (d, q) rotating synchronous frame," in *Proc. 42nd Annu. Conf. IEEE Ind. Electron. Soc.*, 2016, pp. 6323–6328.
[14] S.-H. Hwang and J.-M. Kim, "Dead-time compensation method for voltage-Fed PWM inverter," *IEEE Trans. Energy Convers.*, vol. 25, no. 1, pp. 1–10, Mar. 2010.
[15] D.-M. Park and K.-H. Kim, "Parameter-independent online compensation scheme for dead time and inverter nonlinearity in IPMSM drive through waveform analysis," *IEEE Trans. Ind. Electron.*, vol. 61, no. 2, pp. 701–707, Feb. 2014.
[16] U. Abronzini, C. Attaianese, M. D'Arpino, M. D. Monaco, and G. Tomasso, "Steady-state dead-time compensation in VSI," *IEEE Trans. Ind. Electron.*, vol. 63, no. 9, pp. 5858–5866, Sep. 2016.
[17] Y. Zhao, W. Qiao, and L. Wu, "Dead-time effect analysis and compensation for a sliding-mode position observer-based Sensorless IPMSM control system," *IEEE Trans. Ind. Appl.*, vol. 51, no. 3, pp. 2528–2535, Jun. 2015.
[18] L. Wang, C. T. Freeman, S. Chai, and E. Rogers, "Predictive-repetitive control with constraints: From design to implementation," *J. Process Control*., vol. 23, no. 7, pp. 956–967, Aug. 2013.
[19] J. H. Lee, S. Natarajana, and K. S. Lee, "A model-based predictive control approach to repetitive control of continuous processes with periodic," *J. Process Control*., vol. 11, no. 2, pp. 195–207, Apr. 2001.
[20] M. Gupta and J. H. Lee, "Period-robust repetitive model predictive control," *J. Process Control*., vol. 16, no. 6, pp. 545–555, Jul. 2006.
[21] D. Limon, M. Pereira, D. M. Peña, T. Alamo, C. N. Jones, and M. N. Zeilinger, "MPC for tracking periodic references," *IEEE Trans. Autom. Control*, vol. 61, no. 4, pp. 1123–1128, Jul. 2016.
[22] S.-K. Oh and J. M. Lee, "Iterative learning model predictive control for constrained multivariable control of batch processes," *Comput. Chem. Eng.*, vol. 93, no. 4, pp. 284–292, Oct. 2016.

[23] Y. Gao and K. T. Chong, "The explicit constrained min-max model predictive control of a discrete-time linear system with uncertain disturbance," *IEEE Trans. Autom. Control*, vol. 57, no. 9, pp. 2373–2378, Sep. 2012.
[24] M. Preindl, "Robust control invariant sets and Lyapunov-based MPC for IPM synchronous motor drives," *IEEE Trans. Ind. Electron.*, vol. 63, no. 6, pp. 3925–3933, Jun. 2016.
[25] S.-K. Kim, D.-K. Choi, K.-B. Lee, and Y. I. Lee, "Offset-free model predictive control for the power control of three-phase AC/DC converters," *IEEE Trans. Ind. Electron.*, vol. 62, no. 11, pp. 7114–7126, Nov. 2015.
[26] B. Francis and W. Wonham, "The internal model principle for linear multivariable regulators," *Appl. Math. Optim.*, vol. 2, no. 2, pp. 170–194, May 1975.
[27] A. G. Yepes, F. D. Freijedo, J. Doval-Gandoy, O. Lopez, J. Malvar, and P. Fernandez-Comesana, "Effects of discretization methods on the performance of resonant controllers," *IEEE Trans. Power Electron*., vol. 25, no. 7, pp. 1692–1712, Jan. 2010.
[28] C. Xia, Z. Zhou, Z. Wang, Y. Yan, and T. Shi, "Computationally efficient multi-step direct predictive torque control for surface-mounted permanent magnet synchronous motor," *IET Electr. Power Appl.*, to be published. [Online]. Available: http://digital-library.theiet.org/content/journals/10.1049/iet-epa.2016.0221
[29] W. Gong *et al.*, "Magnetostriction and the influence of harmonics in flux density in electrical steel," *IEEE Trans. Magn.*, vol. 51, no. 11, Nov. 2015, Art. no. 6101404.
[30] A. H. Abosh, Z. Q. Zhu, and Y. Ren, "Reduction of torque and flux ripples in space vector modulation based direct torque control of asymmetric permanent magnet synchronous machine," *IEEE Trans. Power Electron.*, vol. 32, no. 4, pp. 2976–2986, Apr. 2009.
[31] R. Islam, I. Husain, A. Fardoun, and K. McLaughlin, "Permanent magnet synchronous motor magnet designs with skewing for torque ripple and cogging torque reduction," *IEEE Trans. Ind. Appl.*, vol. 45, no. 1, pp. 152–160, Jan./Feb. 2009.
[32] J. Maciejowski, *Predictive Control with Constraints*, Englewood Cliffs, NJ, USA: Prentice-Hall, 2001.
[33] G. F. Franklin, *Digital Control of Dynamic Systems*, Upper Saddle River, NJ, USA: Addison-Wesley, 1980.
[34] L. Wang, *Model Predictive Control System Design and Implementation Using MATLAB*, London, U.K.: Springer-Verlag, 2009, pp. 4–6.

Zhanqing Zhou (S'17) was born in Ningxia, China, in 1989. He received the B.S. and M.S. degrees from Tianjin University, Tianjin, China, in 2010 and 2013, respectively, all in electrical engineering. He is currently working toward the Ph.D. degree in electrical engineering at the School of Electrical and Information Engineering, Tianjin University.

His research interests include electrical machines and their control systems, power electronics, and renewable energy systems.

Changliang Xia (SM'12) was born in Tianjin, China, in 1968. He received the B. S. degree from Tianjin University, Tianjin, China, in 1990, and the M. S. and Ph.D. degrees from Zhejiang University, Hangzhou, China, in 1993 and 1995, respectively, all in electrical engineering.

He is currently a Professor in the School of Electrical and Information Engineering, Tianjin University, and also in Tianjin Engineering Center of Electric Machine System Design and Control, Tianjin Polytechnic University, Tianjin, China. In 2008, he became "Yangtze Fund Scholar" Distinguished Professor and is currently supported by the National Science Fund for Distinguished Young Scholars. His research interests include electrical machines and their control systems, power electronics, and control of wind generators.

Yan Yan was born in Tianjin, China, in 1981. She received the B.S. and M.S. degrees from Tianjin University of Science and Technology, Tianjin, China, in 2004 and 2007, respectively, and the Ph.D. degree from Tianjin University, Tianjin, China, in 2010, all in electrical engineering.

She is currently a Lecturer in the School of Electrical and Information Engineering, Tianjin University. Her research interests include the design and control of matrix converter for electric drive applications and power converters for wind power generation.

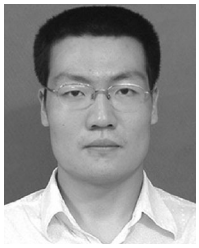

Zhiqiang Wang (M'13) was born in Tianjin, China, in 1984. He received the B.S. degree from Hebei University of Technology, Tianjin, China, in 2002, and the M.S. and Ph.D. degrees from Tianjin University, Tianjin, China, in 2008 and 2012, respectively, all in electrical engineering.

He is currently a Lecturer in the School of Electrical Engineering and Automation, Tianjin Polytechnic University, Tianjin, China. His research interests include electrical machines, power electronics and their control systems.

Tingna Shi (M'13) was born in Zhejiang, China, in 1969. She received the B.S. and M.S. degrees from Zhejiang University, Hangzhou, China, in 1991 and 1996, respectively, and the Ph.D. degree from Tianjin University, Tianjin, China, in 2009, all in electrical engineering.

She is currently a Professor in the School of Electrical and Information Engineering, Tianjin University. Her current research interests include electrical machines and their control systems, power electronics, and electric drives.